

Vacancy and interstitial defects at graphite surfaces: Scanning tunneling microscopic study of the structure, electronic property, and yield for ion-induced defect creation

J. R. Hahn and H. Kang*

Department of Chemistry and Center for Ion-Surface Reaction, Pohang University of Science and Technology, Pohang, Gyeongbuk, South Korea 790-784

(Received 14 December 1998; revised manuscript received 9 April 1999)

Point defects at graphite surfaces are investigated by scanning tunneling microscopy (STM) under ultrahigh vacuum conditions. Graphite surfaces are bombarded with energy-selected beams of Ar^+ and Kr^+ ions at low energies (<100 eV) to generate the defects on atomic scale. The ion bombardment produces mostly carbon vacancy defects (VD's) and interstitial defects (ID's), the latter formed by trapping an incident ion beneath the surface carbon plane. A VD appears as a protrusion in STM image and so does an ID, but they can be distinguished from each other in the measurements of local tunneling barrier height (Φ) and tunneling spectroscopy (I - V curve). They can also be physically separated by heating the defected surface to a temperature high enough to evaporate the noble-gas interstitials. By employing these methodologies, we are able to examine the electronic structure of individual VD's and ID's. A VD exhibits a Φ value substantially lower than an ID or a clean graphite. Both VD and ID increase the local charge density of states near the Fermi energy, but this effect is largest for a VD due to its dangling bonds. A $\sqrt{3}\times\sqrt{3}$ superlattice structure appears from an ID, but not from a VD. This observation disproves the existing theoretical interpretation that the superlattice structure results from electron scattering at a VD site. The absolute yield is measured for production of VD's and ID's at ion impact energies of 40–100 eV. The features of the yield curves, including the dependency on ion energy and the threshold energies for defect creation, provide reasonable explanations for the ion-surface collisional events leading to VD and ID creation in the low-energy regime. [S0163-1829(99)11831-9]

I. INTRODUCTION

Point defects at a surface, consisting of the absence or extra presence of atoms, represent the simplest kind of deviation from a perfect crystal plane. Such defects often have profound influence on the electrical, optical, and chemical properties of a surface. They are an intrinsic feature of a real surface as their presence is a normal thermal equilibrium phenomenon. Experimental findings on point defects, particularly on their electronic and geometrical structures, have been very limited until recently. Because many surface spectroscopic techniques measure properties averaged over a sampling area, it is difficult to deal with the individual defects that are randomly dispersed and have low density on a surface. With the advent of scanning tunneling microscopy (STM),¹ a real-space and near-field probe, it is possible to examine individual defects at a surface. Point defects can be artificially introduced to a surface by bombarding it with energetic ions. Of particular interest in this study is the defects created by low-energy (≤ 100 eV) ions. When the ion energy barely exceeds the threshold value for displacement of surface atoms, the ion-surface collision can remove one or at most a few surface atoms, thus producing mostly point defects on an atomic scale.^{2–9} The defect creation mechanism with such low-energy collisions is intimately related to the film deposition and etching processes using ion beams and plasma. High quality films can be grown through continuous generation and annihilation of atomic defects during ion bombardment of surfaces.^{10,11}

There have been numerous studies involving ion bombardment of solid surfaces and investigation of the ion-

induced damage using STM.^{2–5,12–24} Many of these studies employed high energy (>500 eV) conditions for ion bombardment,^{12–22} and the target materials included Si,¹² PbS,¹³ and graphite.^{14–22} The STM image of a Si surface bombarded with Ar^+ beams at an energy of 700 eV showed hillocks,¹² while craters were observed on PbS upon Kr^+ impact at 8 keV.¹³ On graphite surfaces, only hillocks were observed in the STM image after bombardment with various ions at various impact conditions.^{14–22} The hillocks produced from high-energy ion collisions were large, typically a few nm in diameter or larger.^{14,15,17,19} These hillock structures were interpreted as representing the actual geometry of damaged spots, i.e., local erosion of carbon layers. Several explanations were proposed for the formation of hillocks, including thermal spikes,¹⁴ defect-induced stress,¹⁶ and electronic excitation.¹⁷ While high energy ions generate complex collisional cascades in the solid and the resulting damage extends to a wide region, the ion-surface collisional events can be greatly simplified when ion energy is below 100 eV. Such low-energy ions penetrate only to a shallow depth and the number of atomic displacements is reduced to mainly primary knock-on events.^{6–9} The defects created by low-energy ions on graphite surfaces were recently examined by several researchers.^{3–5,23,24} The STM images of the ion-bombarded surfaces showed hillocks of smaller sizes to a few Å in diameter. Interestingly, these small hillocks originate from an increase in the charge density of states (CDOS) near the Fermi energy level (E_F), but not from a geometric protrusion of a surface.⁴ These studies reported many interesting STM images of point defects, but they had important shortcomings. In the earlier cases, the nature of the defects under investigation was poorly characterized. This hampered

a clear interpretation of the observed STM features, i.e., whether they should be related to vacancies, interstitials, or other types of defects. Also, there was the possibility of impurity adsorption at defect sites when STM measurements were carried out under ambient conditions.

In this paper, we present a comprehensive study of atomic defects at a graphite surface using ultrahigh vacuum (UHV) STM. The defects were created under well-controlled conditions by bombarding a surface with energy-selected beams of Ar^+ and Kr^+ ions in the range of 40–100 eV. They were analyzed *in situ* using UHV-STM. The two types of defects created under this condition, carbon vacancies and noble gas interstitials, were identified and distinguished by thermal heating and scanning tunneling spectroscopy (STS). These experimental features allow a more systematic examination of each type of defect compared with previous studies. The results from our investigation are presented in this paper in the following order. Sec. III A presents the STM topographic image of the defects created by ion impact. Sections III B and III C report the results of STS measurement of the defects. Their electronic properties are investigated and the methods for distinguishing a vacancy defect (VD) and an interstitial defect (ID) are described. Section III D presents the size distribution of defect structures obtained from their appearance statistics in the STM images. Section III E examines the yield for defect creation upon ion impact at various ion energies. Section III F reports our observation of the superlattice structure's appearance around a defect. These experimental results are discussed in Sec. IV in the order of the collisional events leading to defect production (Sec. IV A), the geometric structure of defects (Sec. IV B), the electronic structure (Sec. IV C), and the yield for defect creation by ion impact (Sec. IV D).

II. EXPERIMENTAL

Graphite samples [highly ordered pyrolytic graphite (HOPG), Advanced Ceramics ZYA grade] were cleaved with adhesive tape, and loaded into the STM chamber. The STM chamber was equipped with a home-built UHV-STM, an *e*-beam heater, a thermal evaporator, and a storage assembly for tips and samples. The graphite sample was cleaned by degassing it in a vacuum at 650 °C for several hours and flash annealing to 1000 °C for a few minutes. After checking the surface condition and cleanness with STM, the sample was transferred to the ion-surface collision chamber for ion bombardment experiment. The sample transfer between the STM and ion-surface collision chambers was done maintaining the vacuum environment using the vacuum sample-transfer system. The base pressure of the STM chamber was below 2×10^{-10} Torr.

The ion-surface collision chamber¹¹ consists of an ion source, a beam transport region, a low-energy decelerator, and a UHV analysis chamber equipped with various surface spectroscopic tools. The sample was bombarded with mass- and energy-selected beams of Ar^+ or Kr^+ ions at normal incidence and for the energy range of 40–100 eV. High-energy neutral species contained in the beam were removed by a neutral trap installed in the beamline. The energy resolution for the beam was less than 2 eV [full width at half maximum (FWHM)]. The ion dose was kept low

(1×10^{11} – 5×10^{13} ions/cm²) so that the effects of single ion impacts can be isolated on the surface. The beam was rastered over the sample area for uniform exposure. Differential pumping of the beamline allowed the UHV condition ($< 2 \times 10^{-9}$ Torr) inside the analysis chamber to be maintained during the ion bombardment.

After ion impact, the sample was transferred back to the STM chamber for subsequent STM measurement using the sample-transfer system. The STM tunneling current I was typically 0.1–0.5 nA and a sample bias was within ± 300 mV. A tip was a W-wire electrochemically etched in a KOH solution. The tip was checked for giving good atomic resolution of a topographic image in an undamaged area before and after the scans over the ion-impacted regions. Unless otherwise specified, all the STM measurements reported in this paper were made by UHV-STM. The local barrier height for electron tunneling Φ was measured using the ac modulation method²¹ by applying an ac voltage to the *z*-piezo drive so that the tip oscillates at a low amplitude ($\Delta z < 0.5$ Å) at a frequency of 1–10 kHz. The induced modulation of the tunneling current was measured using a lock-in detection technique. The modulation frequency was within the bandwidth of an *I*-*V* converter. The lock-in output gives $d \ln I/dz$, which is proportional to Φ . Φ was measured two dimensionally (spatially resolved Φ image), and recorded simultaneously with surface topography. The current-to-bias voltage measurement (*I*-*V* spectroscopy)²⁵ was carried out to investigate the electronic structure of defects in the following manner. During a topographic scan over a certain area, a tip stopped at a preselected surface position. The constant-current feedback loop was interrupted, and then the bias voltage was ramped within a specified range in order to obtain *I*-*V* data. After taking the *I*-*V* curve, the feedback loop was reactivated and then the topographic scan restarted. The *I*-*V* curves were recorded from multiple sites in a scan area (from 4×4 to 32×32 sites) intermittently during a topographic scan.

III. RESULTS

A. STM images of ion-induced defects

Upon bombardment of a graphite surface with low energy ions, an STM image shows characteristic features of the ion-induced defects created at the surface. Figure 1 presents the STM images of the defects in two different scales. In the wide-scan (500×500 Å) image of Fig. 1(a), several ion-induced defects appear as bright spots, or hillocks, randomly dispersed on an originally flat surface. The defect features are readily observable in an STM image, and appear rather insensitive to the applied bias voltage and polarity within a range of ± 1 V. By using a low flux of incident ions, each defect is isolated on the surface with negligible defect-defect interactions. The diameter of the bright spots varies from a few Å to several tens of Å. In Fig. 1(a), only large-sized defects are discernible because the scan area is very wide. A defect structure of a small size is presented in Fig. 1(b) with high resolution. The bright spot has a diameter of ~ 3 Å. Except in this region of local brightness, the original graphite pattern is visible in the scan area. Such a small hillock is most frequently observed from a surface impacted by 50–60 eV Ar^+ ions. These STM images, taken under *in situ* UHV

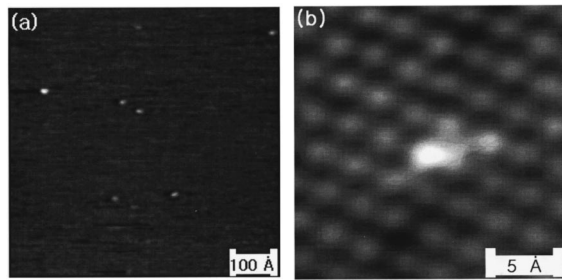


FIG. 1. STM topographic images of the defects created at a graphite surface by Ar^+ ion impact. (a) A large-scale image and (b) a high resolution image. The length inside the white bar corresponds to a bar length. Ion impact energy is 100 eV (a) and 60 eV (b). Scan conditions are sample bias of -100 mV and tunneling current of 0.5 nA (a); sample bias of -60 mV and tunneling current 0.3 nA (b).

conditions, are similar to those obtained under ambient conditions.^{2-5,23,24} The similarity between the STM features observed under UHV conditions and in air indicates that impurity adsorption at a defect site does not significantly alter the bright defect images.

The defect features created in this present work are much smaller in size than those produced by ion bombardment at high energy.^{14,15,17,19} Apparently, mostly atomic-scale defects are produced under the present ion bombardment condition using ion energies close to the threshold of defect formation.^{6,7} Previously, it has been shown³⁻⁷ that these low-energy ions can generate vacancy defects (VD's) in the surface carbon plane as well as interstitial defects (ID's), the latter created by trapping an incident ion underneath the carbon plane. It is impossible to distinguish VD and ID from the STM images of Fig. 1 alone. In the following sections, we examine the STM features of defects in further detail to differentiate VD's and ID's and to probe their structure.

B. Local tunneling barrier height: Differentiation of VD and ID

STM is capable of measuring a local tunneling barrier height. The lateral variation of Φ , or $\Phi(x,y)$ image, can provide a useful means for examining chemical heterogeneity in certain multicomponent surfaces.²⁶⁻²⁸ In this work, the $\Phi(x,y)$ image is measured on a defected graphite surface, simultaneously with STM topographic image by a two-channel experiment (Sec. II). Figures 2(a) and 2(c) show the topographic images and the corresponding $\Phi(x,y)$ images are shown in Figs. 2(b) and 2(d). Clear contrast is evident between the topography and the Φ image. Figures 2(a) and 2(b) are in a pair and correspond to the surface impacted by 100 eV Kr^+ ions. Several of the Kr^+ -induced defects, appearing as hillocks in the topographic image of Fig. 2(a), are imaged as dark spots in the $\Phi(x,y)$ image of Fig. 2(b). The dark spots have Φ values lowered by ~ 0.3 eV compared with an undamaged area. On the other hand, the rest of the defects are not discernible from an undamaged region in the $\Phi(x,y)$ image. These "transparent" defects have Φ values similar to that of clean graphite, which is 3.8 eV in our measurement using a W tip. Figures 2(c) and 2(d) represent the results obtained from a surface impacted with 50 eV Kr^+

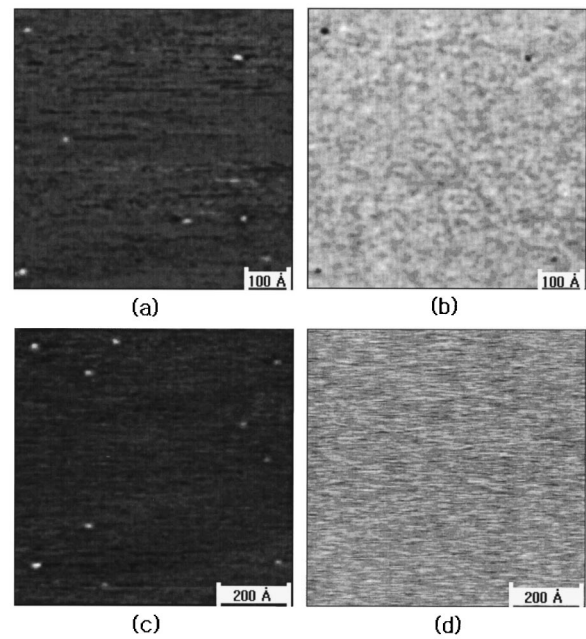


FIG. 2. (a) STM topographic image of a graphite surface impacted with Kr^+ ions at 100 eV. (b) The image of local barrier height obtained from the same region simultaneously with (a). (c) STM topographic image obtained after 50 eV Kr^+ impact. (d) The corresponding image of local barrier height from region (c).

ions. The topographic image of this surface [Fig. 2(c)] shows hillocks, but none of them is visible in the corresponding $\Phi(x,y)$ image [Fig. 2(d)].

According to the threshold measurement presented in Sec. III E, Kr^+ impact at 50 eV produces exclusively ID's on the surface. Therefore, we interpret that ID's are transparent in the $\Phi(x,y)$ image, and the dark spots must represent VD's. We further check this possibility with a sample impacted with 100 eV Kr^+ [Fig. 2(a)], by heating it inside a vacuum at 700°C . This thermal heating procedure removes only ID's from the surface and leaves VD's unaltered (Sec. III D). After heating the surface, we observe 1:1 correspondence between the hillocks of topographic image and the dark spots of Φ image. This result verifies that VD's and ID's can be distinguished by the Φ measurement.

The interpretation of experimental Φ data can be complicated for certain systems. It has been suggested²⁹ that on a soft surface such as graphite, an experimental Φ value can be distorted due to the repulsive forces between a tip and a surface, which results in a lowering of the measured Φ value. However, recent studies³⁰⁻³² show that this effect is insignificant for imaging a graphite surface even in air when a normal imaging condition is employed ($R_t < 10^7 \Omega$), where R_t represents tunneling gap resistance. Another effect might intervene when a surface has an abrupt topographic change, e.g., at a step edge.³³ At such a position the Φ image can be entangled with topography because the angle changes between the direction of tip modulation (z) and the microscopic direction of a tip to a surface atom. Considering that both VD's and ID's appear as protrusions and their sizes are small, the mixing effect of topography and Φ is not expected to be the reason for the observed Φ difference. We believe that the Φ difference reflects a real Φ variation at the VD and ID sites, originating from their different electronic properties.

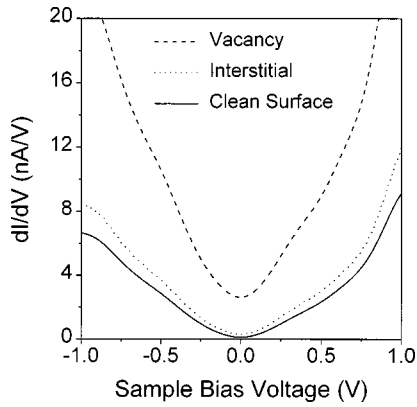


FIG. 3. The conductance curves obtained on a VD, ID(Ar), and undamaged graphite surface. The defects are prepared by impact of 100 eV Ar^+ ions.

C. I - V spectroscopy

The electronic property of VD's and ID's is further examined by measuring the I - V spectroscopy at the defect sites. The I - V spectroscopy is performed intermittently during a topographic scan, in such a way that the I - V data can be labeled with a specific position on the topographic image. For increased reliability, the I - V data are repeatedly taken for each surface position and then averaged. Figure 3 shows the I - V data in the derivative form, or the conductance (dI/dV) curves, measured on VD's, ID's, and in the undamaged region. The data are obtained from a surface impacted by 100 eV Ar^+ ions, which contains VD's as well as ID's. By thermal heating of the surface, VD's can be isolated on the surface (Sec. III D). A comparison of the I - V curves obtained before and after heating of the surface allows separation of the I - V spectra for VD's and ID's. In Fig. 3, the conductance near E_F is greatly increased by the presence of a VD. The conductance value gives a relative measure for local CDOS, when the same tips and scan conditions are used. For a VD, the conductance value at near zero voltage is enhanced by 15–30 times from a clean graphite surface. For an ID, the enhancement is 2–3 times. In comparison, a Pd cluster on a graphite surface increases the local CDOS by 15 times from a clean surface.³⁶ The charge enhancement caused by a VD is comparable to that by a Pd cluster, indicating that graphite undergoes transition from a semimetal to a metallic state. Theoretical calculation³⁷ predicts a resemblance between a metal adatom and a graphite vacancy in their appearance in the STM image, consistent with a metallic state of a VD. No specific band structure is clearly visible within a bias voltage range of ± 1.0 V for a VD's, ID's, and clean graphite. The I - V features on a clean surface is similar to the previous reports.^{38,39} An I - V curve was reported²² for a graphite defect produced by 3.1 keV Au^+ impact, and in this case a CDOS increase of about 3 times was observed. The defect nature, however, was not identified in this study.

D. The size distributions for VD and ID

The size of the hillocks in STM topographic image is statistically analyzed. The statistics is obtained from the measurement of more than three hundred defects. Shown in Figs. 4(a) and 4(b) are the histograms for the diameter and

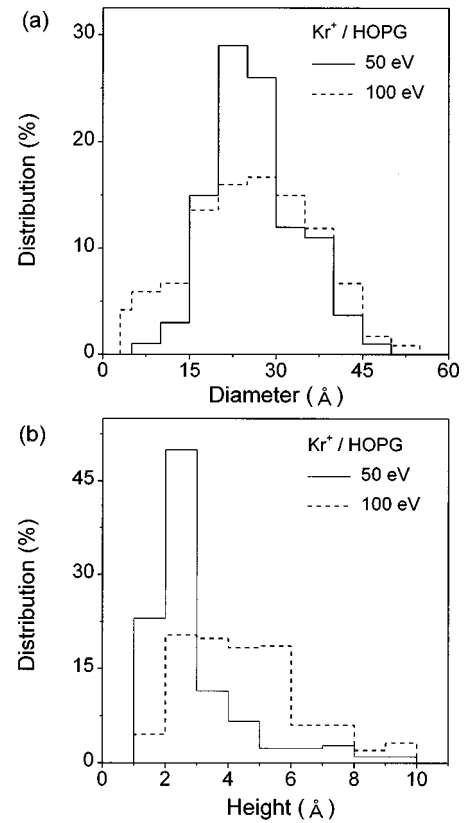


FIG. 4. The size distributions for the hillocks produced by Kr^+ ions at the impact energies of 50 and 100 eV. (a) Diameter distribution. (b) Height distribution.

height of the hillocks, respectively, produced by Kr^+ ions at impact energy of 50 and 100 eV. The distribution for the diameter remains rather unchanged with impact energy, except that it becomes slightly broader at 100 eV. The average diameter is 27 ± 2 Å for all energies, as summarized in Table I. On the other hand, the average height exhibits substantial variation with energy; it is 3.0 ± 0.1 Å for 50–80 eV, suddenly increasing to 3.9 Å at 90 eV and 4.5 Å at 100 eV (Table I). The height distribution becomes significantly broader toward a larger value above 80 eV. The size distribution for Ar^+ -induced defects has been reported in our earlier report.⁵ Table I compares the average diameter and height for the defects generated by Ar^+ and Kr^+ . The Ar^+ -induced defect certainly exhibits a different trend compared with Kr^+ . The defect size created by Ar^+ monotonously increases both in diameter and height with increasing ion energy.

The two defect components on graphite, VD and ID, have different thermal properties, based on which it is possible to

TABLE I. The average height and diameter of the defects produced by Ar^+ and Kr^+ ion impact.

Impact energy (eV)		40	50	60	80	90	100
Average height of STM protrusion (Å)	Ar^+	1.4	2.1	3.5		4.5	
	Kr^+	2.9	3.0	3.0	3.9	4.5	
Average diameter of STM protrusion (Å)	Ar^+	6.3	8.1	13.1		19.5	
	Kr^+	27.8	28.6	29.1	26.6	25.1	

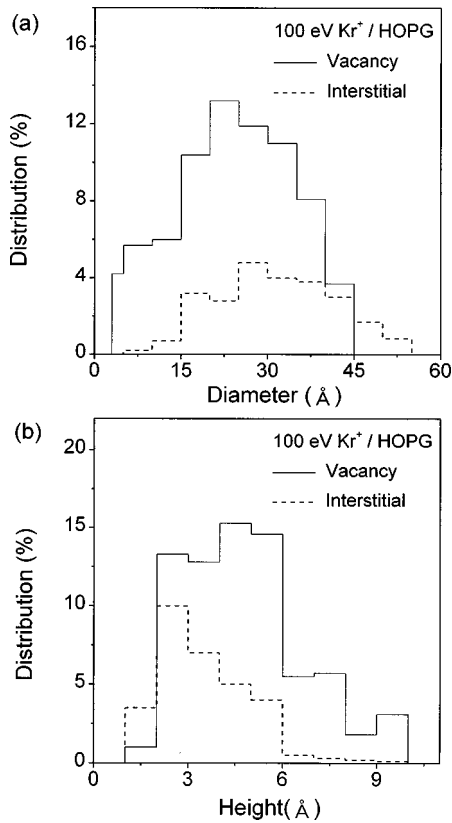


FIG. 5. The size distributions differentiated for VD (solid line) and ID (dashed line). (a) Diameter distribution. (b) Height distribution. The defects are produced by 100 eV Kr^+ impact.

separate one from another. An ID can be removed by heating a sample to a sufficiently high temperature inside a vacuum, such that the trapped noble gas atom is thermally desorbed. The desorption temperature for trapped atoms is 90–100 °C for He, 120–160 °C for Ne, and 200–300 °C for Ar.⁷ For Kr^+ -impacted samples, a heating temperature of 700 °C is observed to be sufficient for removing ID(Kr)'s. At this temperature VD's are assumed not to be destroyed nor newly created. This assumption is reasonable because the formation energy for a single-atom VD on a graphite surface $E^f(\text{VD})$ is 7.44 eV and its migration energy to the a -axis direction (parallel to a carbon plane) $E^{ma}(\text{VD})$ is 3.1 eV.⁴⁰ We have checked the thermal property of VD by further increasing the temperature to 1200 °C, and have not observed any difference in the number of defects counted in STM images. This result verifies that thermal heating does not create nor annihilate VD's on the surface, and removes only ID's.

Figures 5(a) and 5(b) show the size distributions for VD's and ID's at a surface impacted by 100 eV Kr^+ ions. The size distribution for VD is measured after heating a sample. The ID distribution is obtained by subtracting the VD distribution from the total (undifferentiated) defect distribution. A difference is evident in the sizes of VD's and ID's. ID's tend to have a slightly larger diameter than VD's, and a substantially lower height. The size distribution for ID ranges 15–45 Å in diameter and 2–5 Å in height in FWHM. Note that this distribution is close to that for the total defects created by 50–80 eV Kr^+ impact. The reason for such resemblance is that 50–80 eV Kr^+ ions produce exclusively ID's, as will be described in Sec. III E. VD's appear in the STM image as

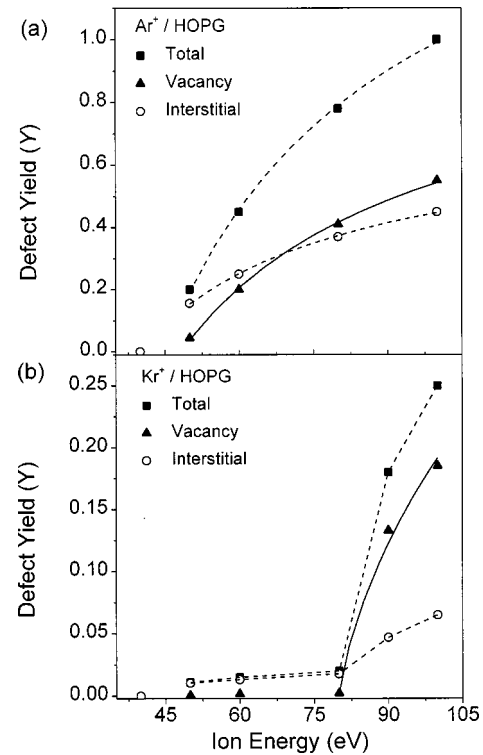


FIG. 6. The production yields of total defect, VD, and ID as a function of ion impact energy for 50–100 eV. (a) Ar^+ impact. (b) Kr^+ impact. The solid line is a fitting by the line-of-center collision model. The dashed line is a guide to the eye.

higher protrusions, the height distribution ranging 2–6 Å in FWHM with a substantial population up to 10 Å.

E. The dependency of VD and ID production rate on ion energy

The defect production yield is measured as a function of ion impact energy for Ar^+ and Kr^+ , and the results are presented in Fig. 6. The yield Y is defined as the ratio of the number of STM protrusions to incident ions. Upon impact of 40 eV Ar^+ and Kr^+ , no STM protrusion is observed and the surface remains unaltered from its original state. This observation means that 40 eV Ar^+ and Kr^+ ions do not create a VD nor ID on the surface. Small hillocks start to appear at the impact energy of 50 eV, a value only a few eV higher than the surface penetration threshold energies reported in the literature: 43.5 ± 1.5 eV for Ar^+ and 47.5 ± 2.5 eV for Kr^+ .⁶ Figure 6 presents the defect production yield distinguished between VD's and ID's together with the total defect yield. The production yield for VD [$Y(\text{VD})$] is measured by using the thermal separation method. The yield for ID [$Y(\text{ID})$] is calculated by subtracting $Y(\text{VD})$ from a total defect yield. The energy dependency of the yield is quite different between Ar^+ and Kr^+ . For the Ar^+ case [Fig. 6(a)], both $Y(\text{VD})$ and $Y(\text{ID})$ increase smoothly with increasing ion energy. ID's are formed more efficiently at energies below 70 eV, but $Y(\text{VD})$ increases more rapidly with increasing energy to become larger at the higher energies. This feature can be rationalized in terms of the different threshold energies between the Ar^+ penetration into a graphite surface and the carbon displacement. The threshold energy for sur-

face penetration is 43.5 ± 1.5 eV with Ar^+ ion and for carbon displacement 47.3 eV.^{6,7} The surface penetration with a lower threshold energy should be more favorable than carbon displacement for low energy collisions. An ID can be created by surface penetration, but VD formation requires carbon displacement. In this regard, ID's should be more efficiently formed at a low energy.

For the case of Kr^+ [Fig. 6(b)], the defect production yield is very low ($<2\%$) up to an impact energy of 80 eV. Thermal heating to 700 °C removes almost all of the defect structures ($>93\%$) formed at these low energies (50–80 eV), revealing that these defects are exclusively ID's. Note that for Kr^+ impact there is a large gap between the threshold energy for surface penetration (47.5 ± 2.5 eV) and for carbon displacement (80.8 eV).⁶ These threshold values are very consistent with our observation that only ID(Kr)'s are created below 80 eV. Above this energy, both $Y(\text{VD})$ and $Y(\text{ID})$ rapidly increase with increasing energy. Therefore, it appears that VD creation by Kr^+ collision accompanies efficient ID production as well, in other words, a Kr^+ ion that hits and knocks off surface carbons tends to become embedded beneath the surface carbon layer. This interpretation is reasonable because Kr^+ is much heavier than carbon. A Kr^+ ion retains a substantial portion of initial momentum even after colliding with surface carbons, penetrating a carbon layer rather than scattering backwards from the surface.

Creation of a VD on a surface is likely to involve direct, impulsive collision between an incident ion and surface atom, leading to ejection of the surface atom. In a theoretical description of such knock-on events, the line-of-centers collision model may provide a simple and appropriate choice.⁴¹ The data for $Y(\text{VD})$ are fitted to the function of the line-of-centers model, which is expressed as

$$Y(\text{VD}) = [1 - E_{\text{th}}(\text{VD})/E_k]^c, \quad (1)$$

where $E_{\text{th}}(\text{VD})$ is the threshold energy for VD production, E_k is ion impact energy, and c is a fitting constant. The solid lines in Fig. 6 represent the functional form of Eq. (1). This model may not be extensible to the ID formation process near the threshold energy, or the ion penetration without irreversible carbon displacement, in which many-body interactions become more important. $E_{\text{th}}[\text{VD}(\text{Ar}^+)]$ is determined to be 48 eV from the fitting of the $\text{VD}(\text{Ar}^+)$ data. This value agrees well with the carbon displacement energy for Ar^+ -graphite collision (47.3 eV) obtained from Auger line shape analysis.⁶ Fitting the $\text{VD}(\text{Kr}^+)$ data for energies of 80 eV and higher, we obtain $E_{\text{th}}[\text{VD}(\text{Kr}^+)] = 80$ eV. The threshold for carbon displacement by Kr^+ collision was reported to be 80.8 eV.⁶

F. Superlattice structure

The presence of a defect on graphite often produces a $\sqrt{3} \times \sqrt{3}$ superlattice pattern around the defect in STM image. Figure 7 exemplifies such an image obtained from a surface impacted with 80 eV Kr^+ . Superlattice patterns similar to Fig. 7 have been reported by several researchers from various types of defects that were considered as adatoms, point defects, steps, and grain boundaries.^{16,23,24,42} It was suggested^{37,42} that the superlattice pattern does not correspond to the atomic positions of graphite, but to the elec-

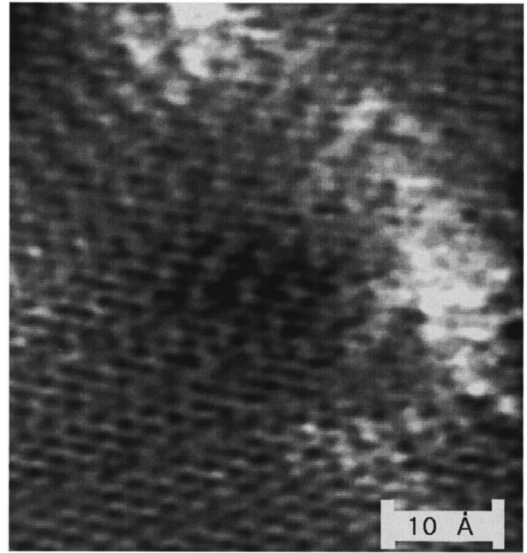


FIG. 7. $\sqrt{3} \times \sqrt{3}$ superlattice patterns appeared on a graphite surface bombarded with 80 eV Kr^+ ions. The bright regions represent defect sites.

tronic perturbation of the surface caused by a defect or adatom. The theoretical interpretation proposed⁴² was that the electronic perturbation has a periodic modulation of wavelength $\sqrt{3}$ times a substrate lattice constant, similar to the Friedel oscillation.

This study is distinguished from previous works, in that point defects are intentionally generated on a graphite under well-controlled ion impact conditions and their nature (VD and ID) is identified. Previous observations were made from natural defects on graphite or poorly identified defect states. The new findings for the superlattice structure, which resulted from this work, are (i) Among the various ion-bombarded surfaces examined, the superlattice patterns are most clearly visible and frequently appear on the surface impacted with 50–80 eV Kr^+ ions. (ii) The existing superlattice features disappear when the sample is heated in vacuum in order to remove ID's. Observations (i) and (ii) indicate that these structures originate from ID's, not from VD's, although the latter were assumed as their origin in the previous interpretation.^{24,42} (iii) Only a certain portion of ID(Kr)'s exhibits the superlattice structure. (iv) The structure is stable for a long period and over repeated scans, when they are found around an ID. (v) They appear in the STM image, but not in AFM image. Item (v) verifies that the superlattice modulation does not correspond to the geometry of surface atoms.

IV. DISCUSSION

A. Collisional events

The interactions of low-energy noble gas ions with a graphite surface have been investigated by using various methods, including classical trajectory simulation (CTS),⁷ thermal desorption mass spectrometry,⁷ Auger electron spectroscopy (AES),^{6,9,43} and molecular dynamics simulation based on *ab initio* potential.⁴⁴ According to the results of

these investigations, the low-energy ion-graphite collision leads to the following three major consequences.

(1) An incident ion back scatters from a surface without producing any damage on the surface. This occurs when the collision energy is lower than the threshold energy of surface penetration or carbon displacement, or when the geometry of ion impact is unfavorable for defect generation.

(2) An ion penetrates a surface carbon layer, but does not create permanent damage on the surface. According to the CTS,⁷ an Ar atom with energy greater than 42 eV can penetrate a graphite surface through the center of a hexagonal ring without irreversibly displacing carbon atoms. The Ar atom then becomes trapped between the basal planes, generating an ID(Ar). The penetration depth of Ar is limited to the first carbon layer when incident energy is below 100 eV.⁷ Kr probably has a penetration range of a similar or slightly shallower depth due to its larger size. For this reason, we can safely assume that the ID's in the present work have interstitial atoms mostly between the first and second carbon layers. An ID(Ar) or ID(Kr) remains stable for a long time (at least several days) at room temperature in vacuum due to a large energy barrier for interstitial diffusion parallel to a basal plane [$E^{ma}(\text{ID}) > 0.2$ eV for Ar].⁷

(3) Ion collision displaces one or a few surface carbon atoms permanently via knock-off events to create a VD. The removed carbon atom can result in three consequences. First, the carbon can be knocked into the interspace between the basal planes of graphite, creating a Frenkel pair. Second, it can be sputtered away from the surface. Third, it can be bonded to surface carbons, for example, generating a three-fold coordinated vertical ring (*D3* defect).⁴⁴ The interstitial carbon atom generated via the first route has a low energy barrier for diffusion along the basal plane direction, such that it is mobile even at room temperature.⁴⁰ In particular, the carbon interstitials generated by the recoil processes have high kinetic energy, and thus they can diffuse a long distance and eventually desorb through a line step. Annihilation of the Frenkel pair is also possible during the diffusion. It has recently been reported²⁰ that the carbon interstitials can cluster together in the interlayer space, when He⁺ bombardment is employed at an excessive dose, high impact energy, and elevated substrate temperature. Such clustering, however, is not expected to occur in the present case because the carbon interstitials have very low concentration. The presence of the *D3* defect was suggested from molecular dynamics calculation,⁴⁴ but its abundance was predicted to be very low (<1%) below a carbon recoil energy of 300 eV. Noble gas interstitials can also be created along with VD's by trapping and neutralization of a projectile ion after carbon displacement. Such ID production will occur more efficiently with Kr⁺ than with Ar⁺, as Kr⁺ is heavier and retains a higher portion of initial momentum after knock-off collision with the surface.

To summarize the ion-surface collisional phenomena discussed above, the ion impact condition employed in the present work created mostly two kinds of defects, VD's and ID's (noble gas). The VD's were formed predominantly in the first carbon layer, and the ID's between the first and second layers. The other types of defects, including carbon interstitials and *D3* defects, were negligible in number.

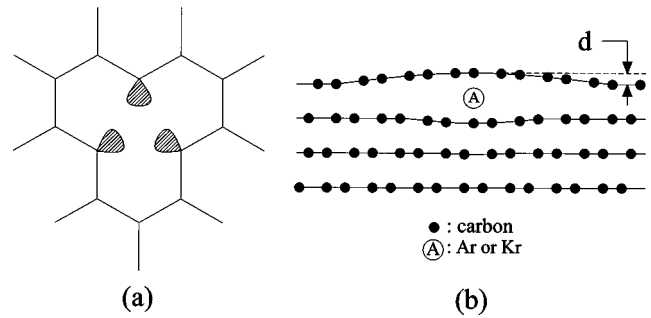


FIG. 8. (a) Simplified drawing of a single-atom vacancy in graphite. The solid line represents C-C network and the three hatched balloons indicate carbon dangling bonds. (b) A side view of an ID formed by trapping of foreign atom A. d represents the distance of carbon plane deformation caused by a trapped atom.

B. The geometric structure of defects

We discuss the geometric structure of defects in this section, and their electronic structure in the next section. Our earlier study using combined STM and AFM (Ref. 4) has revealed that the defects produced by low-energy ion impact have almost flat geometry, although they appear as protrusions in the STM image. The spatial resolution of current AFM technology is insufficient for detecting the hollow site of an atomic VD or the slight deformation of the carbon plane caused by an ID, especially when the defect sites are randomly distributed at a surface. The geometric structures for VD's and ID's produced at a graphite plane are schematically presented in Fig. 8. A single-atom VD has three carbon dangling bonds at the VD site [Fig. 8(a)], and the rest of the carbon network maintains nearly a flat geometry.^{4,34,35} The dangling bonds cause enhancement of local CDOS near E_F in the atoms surrounding the defect.^{4,21,34,44,45} The high protrusion in the STM image comes from this charge increase effect.

Figure 8(b) shows the structure for an ID, in which a noble gas atom is trapped between the first and second carbon planes. The diameter of Ar (3.8 Å) or Kr (4.1 Å) is larger than the graphite interlayer spacing (3.35 Å), and so these atoms cause elastic deformation of graphite basal planes. The deformed surface layer can be detected as a protrusion in STM topography. Molecular modeling calculation^{3,6} shows that the maximum deformation of the surface layer to the c axis [d in Fig. 8(b)] is 0.9 Å for ID(Ar) and 1.1 Å for ID(Kr) for the case of single-atom trapping. In the STM experiment, the average height is measured to be 1.4 Å for ID(Ar) and 3.0 Å for ID(Kr). These numbers are taken from the protrusions generated by 50 eV Ar⁺ and 50–80 eV Kr⁺, respectively (Table I), the conditions that create mostly single-atom ID's. Rabalais and co-workers³ reported a domelike feature in the STM image, which was attributed to an ID(Ar), with a height of 1.0–1.4 Å and diameter 16–20 Å in FWHM. These experimental ID heights might be considered agreeable with the calculated deformations. But there certainly exists a noticeable gap between the STM heights and the calculations, which are larger than measurement uncertainty, and the experimental height is always larger. This extra height of STM protrusion is more pronounced for ID(Kr) than for ID(Ar). Since the molecular modeling accounts for only geometrical deformation, the ex-

tra height has to be attributed to additional electronic effect. The possible origins of the electronic effect will be discussed in Sec. IV C.

The geometric structure of VD cannot properly be deduced from an STM image, because the image is dominated by the effect of charge increase at a VD. As an alternative guide for estimating VD size, we consider the energetics for VD creation by ion collision. Ar^+ collision at 50 eV can remove one surface carbon at most and can produce only a single-atom VD, as this energy is only barely above the threshold for carbon displacement (47.3 eV) and the extra energy is insufficient to remove an additional carbon atom [$E^f(\text{VD})=7.44$ eV (Ref. 40)]. The VD's formed at this energy indeed frequently exhibit the smallest STM features (3–4 Å in diameter). For higher energy, it becomes energetically more feasible to produce a multiatom VD. This agrees with the observation that the size distribution of hillock shifts to a larger value with increasing Ar^+ energy. The degree of charge enhancement is predicted³⁴ to increase with the number of missing atoms. VD(Kr)'s are usually large (2–6 Å in height and 10–40 Å in diameter; Fig. 5), even when they are produced near the threshold energy. This implies that multiatom VD's are more frequently formed by Kr^+ impact than by Ar^+ impact, because Kr^+ has a larger diameter and the impact energy employed for VD production is higher (>80 eV).

C. The electronic structure

The STM signature of a VD has a diameter ranging from 3 to 45 Å, although the actual geometric size of a VD is much smaller, e.g., one or at most a few missing atoms. Apparently, the CDOS increase in the surface atoms surrounding a VD is the reason for the large STM protrusion. This conclusion has been reached in our previous study using STM and AFM.⁴ The CDOS increase occurs in both filled and empty electronic states near E_F . The electronic structure calculation³⁴ also supports this finding. The STM protrusions of the smallest size (3–4 Å in diameter) indicate the CDOS increase in the nearest-neighbor carbon atoms. Such small protrusions are most frequently observed when Ar^+ collision energy is close to the carbon displacement threshold (50–60 eV), implying that they represent single-atom VD's. Large VD features become more abundant at higher collision energy. The largest ones, with a diameter of 45 Å, for example, encompass about 600 surface carbon atoms. The CDOS increase apparently extends to an enormously wide area, a phenomenon that has not been predicted by theory. The I - V spectroscopic data presented in Sec. III C give additional information on the local CDOS. A VD increases the local CDOS near E_F by 15 times compared with a clean graphite surface. Such a degree of CDOS enhancement is as large as that for a Pd metal cluster deposited on graphite,³⁶ indicating a metallic character of graphite VD.

A VD exhibits a lower value of Φ than a clean graphite surface or ID, and appears dark in the $\Phi(x,y)$ image (Fig. 2). Φ is a measure for the decay rate of electron wave functions away from a surface, κ [Eq. (2)].²⁵

$$\Phi = \hbar^2 \kappa^2 / 2m, \quad (2)$$

where m is the electron mass. The low Φ for a VD means slow decay of the wave functions at a VD, and in turn, a large size for the electronic orbitals. A VD has several dangling bonds in place of the missing carbon atoms, and the size of the dangling orbital is significantly larger than a C-C bonding orbital of graphite. We believe that these dangling bonds result in the low Φ . An ID does not have such dangling bonds, and thus can be clearly distinguished from a VD in $\Phi(x,y)$ measurement.

The domelike STM image of ID is interpreted to result from electronic effect as well as geometric deformation of a graphite basal plane, as described in the previous section. The electronic elevation of ID in STM image implies an increase of the local CDOS in the carbon plane directly above a trapped atom. The I - V spectroscopy of Sec. III C gives a quantitative measure for the CDOS increase. ID(Ar) increases the CDOS near E_F by 2–3 times from a clean graphite surface, which is much weaker than VD. The smaller degree of CDOS increase caused by ID is consistent with the small electronic elevation in STM image (0.5–1.9 Å).

We consider two possible causes for the CDOS increase at an ID site. One is the strain in the basal plane introduced by geometric deformation. The valence electronic structure of a graphite basal plane is described by the σ (sp^2) band with partial DOS of σ_s and σ_p and the π band arising from overlap of the p_z orbitals.⁴⁶ Deformation of the plane causes the distortion or weakening of interaction within the σ (sp^2) band and the π band. This leads to a narrowing of the pseudo-band-gap of graphite and to increased CDOS near E_F . That is, the deformation reduces the energy separation of the π (bonding) and π^* (antibonding) bands. Theoretical calculation for randomly distributed sp^2 carbon network⁴⁷ shows a smooth distribution of the π electronic states near E_F , i.e., increase of local CDOS from an undamaged graphite. An embedded Kr atom will cause higher distortion in the bands than Ar due to its larger size, and thus higher local CDOS enhancement, in agreement with the experimental observation. The highest degree of the distortion can be attained by C-C bond breakage, or presence of a VD. Naturally, the charge enhancement effect is largest for VD.

The other possible cause is the electronic disturbance introduced by a trapped atom. There exists weak electronic interaction between the basal planes through overlapping of p_z orbitals. This interaction is crucial for the weak metallic property of graphite. Also, it is generally regarded as the reason for appearance of the trigonal pattern in the STM image of graphite,³⁸ although this issue is not yet fully resolved.^{48,49} The presence of an inert gas atom between the graphite layers can physically block the overlapping of p_z orbitals, thereby changing the CDOS of the p_z orbitals located near an embedded atom. It has been shown^{50,51} that intercalant alkali metal atoms cause disruption of the electronic interaction between the basal planes. The metal atoms can also produce a charge density wave (CDW) through direct electronic interaction (charge transfer) between the carbons and the intercalants. For the case of Ar and Kr interstitials, however, it is questionable that the direct electronic interaction is strong enough to produce a CDW-like effect.

The $\sqrt{3} \times \sqrt{3}$ superlattice structure observed in the STM image (Sec. III F) shows interesting characteristics of ID.

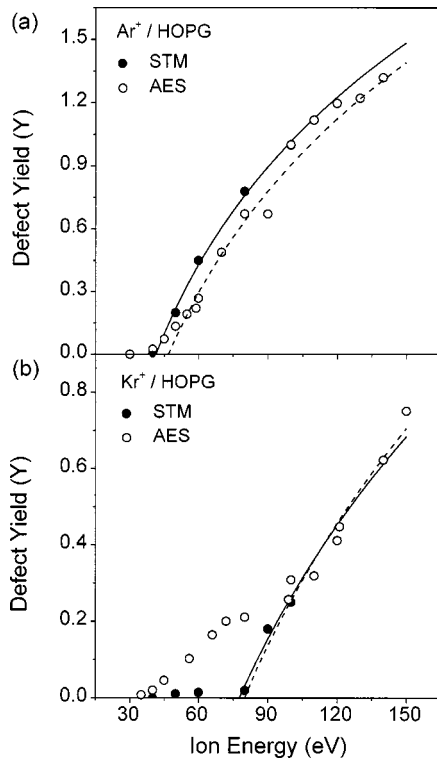


FIG. 9. Comparison of the yield curves for total defect production obtained by STM counting and AES line shape analysis. (a) Ar^+ impact. (b) Kr^+ impact. The yield from the AES measurement is scaled to match the absolute yield obtained by STM counting. The lines show logarithmic fits to the data.

The statistics for the appearance of this structure shows a good reason to believe that it originates from an ID, not from a VD. Note that the previous works reporting such a structure did not distinguish VD's and ID's.^{16,23,24,42} Electron scattering from a defect site was proposed as a possible origin of the superlattice structure.^{24,42} The scattering center determines the modulation intensity and the direction of electronic perturbation. According to this interpretation, however, a VD would be able to generate an electronic perturbation stronger than or at least comparable to an ID. But our observation reveals the opposite. Therefore, theoretical interpretation of the superlattice structure is still unresolved. Only a certain portion of ID's generates the superlattice structure. This observation suggests a possibility that it is related to the location of an interstitial atom inside an inter-layer space at different symmetry sites.

D. The yield curve

A unique feature of Fig. 6 is that the yield is measured separately for VD's and ID's. The yield also represents a quantitative and absolute measure, as the number of defect is directly counted from the STM images.

The yield for total defect production has previously been measured by Rabalais and co-workers using AES line shape analysis.^{6,9,43} Figure 9 compares the total defect yields obtained from the AES method⁶ and from the STM counting method. Considering that the former method gives a relative measure for the yield, we use our STM data as a reference for the absolute yield. The two methods give agreeable yield

TABLE II. The threshold ion impact energies, in eV, for the production of VD's and ID's on a graphite surface measured by different methods.

Defect	STM	AES line shape ^a	CTS ^b
VD(Ar)	48	47.3	
ID(Ar)	38 ^c –41 ^d	43.5	42
VD(Kr)	80	80.8	
ID(Kr)	41 ^c	47.5	

^aReferences 6, 9, and 43.

^bReference 7.

^cObtained by fitting the ID yield curve (Fig. 6).

^dObtained by fitting the total defect yield.

curves for Ar^+ data, except that the AES data exhibit a slight discontinuity at impact energy of 60 eV. For Kr^+ data there exists clear discrepancy between the two methods in the region of 40–80 eV. The yield obtained by STM is very small below 80 eV, while this portion of the curve is amplified in the AES data. In the following, we discuss these yield curves, comparing the significances of the two measurements.

The AES method uses a defect signature appearing in the carbon *KLL* Auger line shape.^{6,9} The change in the carbon line shape, resulting from the development of disorder in a graphite lattice, reveals relative density of surface damage. However, it does not distinguish between VD and the lattice strain caused by an ID, as was pointed out by the authors.⁶ A VD induces a different amount of lineshape change from an ID, and also the contribution by an ID varies depending on the degree of surface deformation, or the size of an interstitial atom. In this regard, the yield curves from the AES and STM methods require different interpretations. The AES yield curve for Kr^+ at 50–80 eV is much higher than the STM curve (Fig. 9). In this region most of the defects are ID(Kr) (Fig. 6). Since an interstitial Kr atom induces surface deformation extending to a large area,⁶ the AES measurement gives possibly an overestimated ID(Kr) yield. The STM counting gives a more accurate yield for this case. The opposite effect may occur for Ar^+ data. The low-energy portion of the AES curve, which constitutes largely ID(Ar) (Fig. 6), has an area slightly smaller than the STM curve. It can be interpreted that an Ar atom induces a smaller degree of surface deformation, and the AES method gives a lower ID(Ar) yield.

Recognizing the different aspects of the STM and AES measurements, we find that the yield curves obtained by the two methods have consistency. Table II summarizes the threshold energies for defect production measured from STM counting, AES line shape analysis,^{6,9,43} and CTS.⁷ The threshold for VD is determined by fitting Eq. (1) to the VD yield curve (Sec. III E). The threshold for ID is obtained by using a logarithmic curve fitting.⁶ For the case of ID(Kr), we take only the curve region below the break point (≤ 80 eV), which corresponds to ID(Kr) formation without VD's. The threshold energies thus obtained for VD are in excellent agreement with the AES result. The threshold energies for ID are obtained to be lower than the AES values by a few eV. Careful examination of the AES data reveals weak tail-

ing even below the threshold energies of the fitting function (Fig. 9), suggesting that the true threshold energies can be lower.

V. CONCLUSIONS

We have investigated the atomic-scale point defects created at a graphite surface by low-energy impact of Ar^+ and Kr^+ ions. The two kinds of defects, VD's and ID's, are separately identified and their properties are examined by STM. The significant findings made from this study are summarized in the following.

(i) Collision of Ar^+ and Kr^+ ions onto a graphite surface at low energy produces VD's and ID's on the surface. Both types of defects are detected as protrusions in STM topographic image. A VD can be distinguished from an ID by the difference in their Φ values and I - V characteristics. A VD exhibits a lower Φ value than an ID and clean surface due to the presence of dangling bond orbitals. VD's can also be physically separated from ID's by heating a surface and evaporating embedded noble-gas atoms.

(ii) The protruded STM image of a VD results from increased local CDOS at the energies near E_F . The CDOS increase is largest for a VD due to its dangling bonds. I - V spectroscopy reveals a CDOS increase of 15–30 times at a VD compared with a clean graphite surface, indicating transition from a semimetal to metallic state. The CDOS enhancement is extended to the neighboring surface atoms, ranging from the nearest-neighbor atoms to several hundred

atoms depending on the number of missing carbon atoms in a VD.

(iii) An ID enhances the CDOS to a lesser degree, for example, 2–3 times for an ID(Ar) compared with an undamaged surface. The increased CDOS, however, contributes a substantial height to the domelike STM image of an ID, in addition to the geometric elevation of a surface carbon plane caused by an interstitial atom. An interstitial Kr induces larger CDOS enhancement and surface deformation than Ar.

(iv) The $\sqrt{3} \times \sqrt{3}$ superlattice structure appears in the STM image of ID, but not in the VD image. This observation calls for new theoretical interpretation for the superlattice structure, disproving the existing model that a VD acts as a scattering center of surface electrons.

(v) The absolute yields for production of VD and ID are measured as a function of ion impact energy, and their formation threshold energies are determined. The threshold energy for ID creation is lower than that for VD creation by only several eV for the case of Ar^+ impact, while Kr^+ exhibits a large difference in the two threshold energies. The features of the yield curves allow reasonable description for the ion-surface collisional events leading to production of VD's and ID's in the low-energy regime.

ACKNOWLEDGMENT

This work was supported by the Creative Research Initiatives Project of the Ministry of Science and Technology, Republic of Korea and by KOSET (98-0501-0101-3).

*Author to whom correspondence should be addressed. FAX: +82-562-279-8157. Electronic address: surfion@postech.ac.kr

¹G. Binnig, H. Rohrer, Ch. Gerber, and E. Weibel, *Phys. Rev. Lett.* **49**, 57 (1982).

²H. Kang, K. H. Park, C. Kim, B. S. Shim, S. Kim, and D. W. Moon, *Nucl. Instrum. Methods Phys. Res. B* **67**, 312 (1992).

³D. Marton, H. Bu, K. J. Boyd, S. S. Todorov, A. H. Al-Bayati, and J. W. Rabalais, *Surf. Sci.* **326**, L489 (1995).

⁴J. R. Hahn, H. Kang, S. Song, and I. C. Jeon, *Phys. Rev. B* **53**, R1725 (1996).

⁵J. R. Hahn and H. Kang, *Surf. Sci.* **357-358**, 165 (1996).

⁶D. Marton, K. J. Boyd, T. Lytle, and J. W. Rabalais, *Phys. Rev. B* **48**, 6757 (1993).

⁷W. Choi, C. Kim, and H. Kang, *Surf. Sci.* **281**, 323 (1993).

⁸C. Kim, H. Kang, and S. C. Park, *Nucl. Instrum. Methods Phys. Res. B* **95**, 171 (1995), and references cited therein.

⁹H. J. Steffen, D. Marton, and J. W. Rabalais, *Phys. Rev. Lett.* **68**, 1726 (1992).

¹⁰Y. Lifshitz, S. R. Kasi, and J. W. Rabalais, *Phys. Rev. B* **41**, 10 468 (1990).

¹¹K. H. Park, B. C. Kim, and H. Kang, *J. Chem. Phys.* **97**, 2742 (1992).

¹²R. M. Feenstra and G. S. Oehrlein, *Appl. Phys. Lett.* **47**, 97 (1985); R. M. Feenstra and G. S. Oehrlein, *J. Vac. Sci. Technol. B* **3**, 1136 (1985).

¹³I. H. Wilson, N. J. Zheng, U. Knipping, and I. S. T. Tson, *Phys. Rev. B* **38**, 8444 (1988).

¹⁴Q. Yang, T. Li, B. V. King, and R. J. MacDonald, *Phys. Rev. B* **53**, 3032 (1996); T. Li, B. V. King, R. J. MacDonald, G. F. Cotterill, D. J. O'Connor, and Q. Yang, *Surf. Sci.* **312**, 399 (1994).

¹⁵R. Coratger, A. Claverie, F. Ajustron, and J. Beauvillain, *Surf. Sci.* **227**, 7 (1990).

¹⁶L. Porte, C. H. de Villeneuve, and M. Phaner, *J. Vac. Sci. Technol. B* **9**, 1064 (1991).

¹⁷F. Thibaudau, J. Cousty, E. Balanzat, and S. Bouffard, *Phys. Rev. Lett.* **67**, 1582 (1991).

¹⁸R. Coratger, A. Claverie, A. Chahboun, V. Landry, F. Ajustron, and J. Beauvillain, *Surf. Sci.* **262**, 208 (1992).

¹⁹K. P. Reimann, W. Bolse, U. Geyer, and K. P. Leib, *Europhys. Lett.* **30**, 463 (1995).

²⁰M. Kappel, M. Steidl, J. Biener, and J. Küppers, *Surf. Sci.* **387**, L1062 (1997).

²¹K. Mochiji, S. Yamamoto, H. Shimizu, S. Ohtani, T. Seguchi, and N. Kobayashi, *J. Appl. Phys.* **82**, 6037 (1997).

²²H. Ogiso, W. Mizutani, S. Nakano, H. Tokumoto, and K. Yamana, *Appl. Phys. A: Mater. Sci. Process* **66**, S1155 (1998).

²³G. M. Shedd and P. E. Russell, *J. Vac. Sci. Technol. A* **9**, 1261 (1991).

²⁴K. F. Kelly, D. Sarkar, G. D. Hale, S. J. Oldenburg, and N. J. Halas, *Science* **273**, 1371 (1996).

²⁵R. Wiesendanger, *Scanning Probe Microscopy and Spectroscopy* (Cambridge University Press, Cambridge, UK, 1994), p. 138.

²⁶G. Binnig and H. Rohrer, *Surf. Sci.* **126**, 236 (1989).

²⁷R. Wiesendanger, L. Eng, H. R. Hidber, P. Oelhafen, L. Rosenthaler, U. Staufer, and H.-J. Güntherodt, *Surf. Sci.* **189/190**, 24 (1987).

²⁸E. Kishi, H. Matusda, R. Kuroda, K. Takimoto, A. Yamano, K. Eguchi, K. Hatanaka, and T. Nagagiri, *Ultramicroscopy* **42-44**, 1067 (1992).

²⁹J. H. Coombs and J. B. Pethica, *IBM J. Res. Dev.* **30**, 443 (1986).

- ³⁰Y. A. Hong, J. R. Hahn, and H. Kang, *J. Chem. Phys.* **108**, 4367 (1998).
- ³¹J. R. Hahn, Y. A. Hong, and H. Kang, *Appl. Phys. A: Mater. Sci. Process.* **66**, S467 (1998).
- ³²H. J. Mamin, E. Ganz, D. W. Abraham, R. E. Thomson, and J. Clarke, *Phys. Rev. B* **34**, 9015 (1986).
- ³³J. M. Gomez-Rodriguez, J. Gomez-Herrero, and A. M. Baro, *Surf. Sci.* **220**, 152 (1989).
- ³⁴K. H. Lee, H. M. Lee, H. M. Eun, W. R. Lee, S. Kim, and D. Kim, *Surf. Sci.* **321**, 267 (1994).
- ³⁵S. M. Lee, Y. H. Lee, Y. G. Hwang, J. R. Hahn, and H. Kang, *Phys. Rev. Lett.* **82**, 217 (1999).
- ³⁶A. Bifone, L. Casalis, and R. Riva, *Phys. Rev. B* **51**, 11 043 (1995).
- ³⁷N. Takeuchi, J. Valenzuela-Benavides, and L. M. de la Garza, *Surf. Sci.* **380**, 190 (1997).
- ³⁸A. Selloni, P. Carnevali, E. Tosatti, and C. D. Chen, *Phys. Rev. B* **31**, 2602 (1985).
- ³⁹N. Li and S. Xie, *Surf. Sci.* **293**, L871 (1993).
- ⁴⁰P. A. Throver and R. M. Mayer, *Phys. Status Solidi A* **47**, 11 (1978).
- ⁴¹R. D. Levine and R. B. Bernstein, *Molecular Reaction Dynamics* (Clarendon, Oxford, 1974).
- ⁴²H. A. Mizes and W. A. Harrison, *J. Vac. Sci. Technol. A* **6**, 300 (1988); H. A. Mizes and J. S. Foster, *Science* **244**, 559 (1989).
- ⁴³D. Marton, K. J. Boyd, T. E. Lytle, and J. W. Rabalais, *Surf. Sci.* **282**, 113 (1993).
- ⁴⁴K. Nordlund and J. Keinonen, *Phys. Rev. Lett.* **77**, 699 (1996).
- ⁴⁵M. R. Soto, *J. Microsc.* **152**, 779 (1988).
- ⁴⁶J. S. Murday, B. I. Dunlap, F. L. Huston II, and P. Oelhafen, *Phys. Rev. B* **24**, 4764 (1981).
- ⁴⁷J. Robertson and E. P. O'Reilly, *Phys. Rev. B* **35**, 2946 (1987).
- ⁴⁸M.-H. Whangbo, W. Liang, J. Ren, S. N. Magonov, and A. Wawkuszewski, *J. Phys. Chem.* **98**, 7602 (1994).
- ⁴⁹A. L. Tchougreeff, *J. Phys. Chem.* **100**, 14048 (1996).
- ⁵⁰H. Dai and C. M. Lieber, *Annu. Rev. Phys. Chem.* **44**, 237 (1993), and references cited therein.
- ⁵¹D. Anselmetti, R. Wiesendanger, and H.-J. Güntherodt, *Phys. Rev. B* **39**, 11 135 (1989).